

Enhanced metrology at the critical point of a many-body Rydberg atomic system

Dong-Sheng Ding^{1,2,3,*,\dagger}, Zong-Kai Liu^{1,2,3,*}, Bao-Sen Shi^{1,2,3,\ddagger},
Guang-Can Guo^{1,2,3}, Klaus Mølmer^{4,\S}, and Charles S. Adams^{5,\P}

¹CAS Key Laboratory of Quantum Information, University of Science and Technology of China, Hefei 230026, China

²CAS Center for Excellence in Quantum Information and Quantum Physics,
University of Science and Technology of China, Hefei 230026, China

³Hefei National Laboratory, University of Science and Technology of China, Hefei 230088, China

⁴Aarhus Institute of Advanced Studies, Aarhus University,
Høegh-Guldbergs Gade 6B, DK-8000 Aarhus C, Denmark
Center for Complex Quantum Systems, Department of Physics and Astronomy,
Aarhus University, Ny Munkegade 120, DK-8000 Aarhus C, Denmark and

⁵Department of Physics, Durham University, South Road, Durham DH1 3LE, United Kingdom
(Dated: July 28, 2022)

The spectral properties of an interacting many-body system may display critical character and have potential applications in precision metrology. Here, we demonstrate such many-body enhanced metrology for microwave (MW) electric fields in a non-equilibrium Rydberg atomic gas. Near criticality the high sensitivity of Rydberg atoms to external MW electric fields, combined with many-body enhancement induces significant changes in the optical transmission. We quantify this behavior using the Fisher information. For continuous optical transmission at the critical point, the Fisher information is three orders of magnitude larger than in independent particle systems, the measured data provides an equivalent sensitivity of $49 \text{ nV/cm/Hz}^{1/2}$. The reported results constitute a milestone towards the application of many-body effects in precision metrology.

INTRODUCTION

Ensembles of well-controlled neutral atoms are ideal systems to explore many-body physics [1–4]. In particular, the controllable interactions among highly-excited Rydberg atoms hold promise for studies of quantum information and many-body physics [5–7]. Benefiting from the large interaction volume of Rydberg atoms, a small change in the Rydberg state population can induce a global macroscopic phase transition between non-interacting (NI) and interacting (I) phases [8]. Laser-induced density-dependent energy shifts of Rydberg states offer a convenient platform to directly observe non-equilibrium phase transitions and bistability [7, 9–12],

and to study dynamical analogues of forest fire [8] and epidemic spreading [13, 14]. In contrast to other optically bistable systems [15–19], Rydberg ensemble experiments can be performed without the need of optical cavity feedback and cryogenic temperatures.

Exploring the non-equilibrium dynamics of the Rydberg system under external fields is intriguing. The emergent thermodynamic and spectroscopic properties of a many-body system of interacting Rydberg atoms present open questions both in theory [11, 20–23] and experiments [7, 8]. Due to the large dipole moment, the Rydberg atoms are highly sensitive to system noise and external electric fields [24–29]. Most dramatically, the macroscopic change in the optical response near a critical point [8, 12] presents a resource for increased metrological sensitivity [30–40]. Accompanying the divergent susceptibility near the critical point, optical probing of the system is highly sensitive to small variations of physical parameters. Critical systems may thus display sensing errors with a generic scaling $\sim 1/\sqrt{N\gamma t^\lambda}$ with $\gamma, \lambda > 1$ [37, 41, 42], where N is the number of atoms and t is the measurement time.

In this article, we demonstrate how Rydberg criticality provides a method for high-sensitivity probing of external parameters. We exploit the extreme sensitivity of the optical transmission at the critical point to probe external MW fields. Due to the critical slowing down near phase transitions, we need to take into account how the system dynamics do not adiabatically follow the stationary state, but rather smooths the system response. This leads to a non-integer power dependence of the Fisher Information (FI) on the duration of the detuning scans. The behavior around criticality is observed to enhance the FI by a factor of up to more than 10^3 compared to a non-interacting ensemble.

RESULTS

Many-body metrology model. We consider a model of N interacting two-level atoms with a ground

* These authors contributed equally to this work.

\dagger dds@ustc.edu.cn

\ddagger drshi@ustc.edu.cn

\S moelmer@phys.au.dk

\P c.s.adams@durham.ac.uk

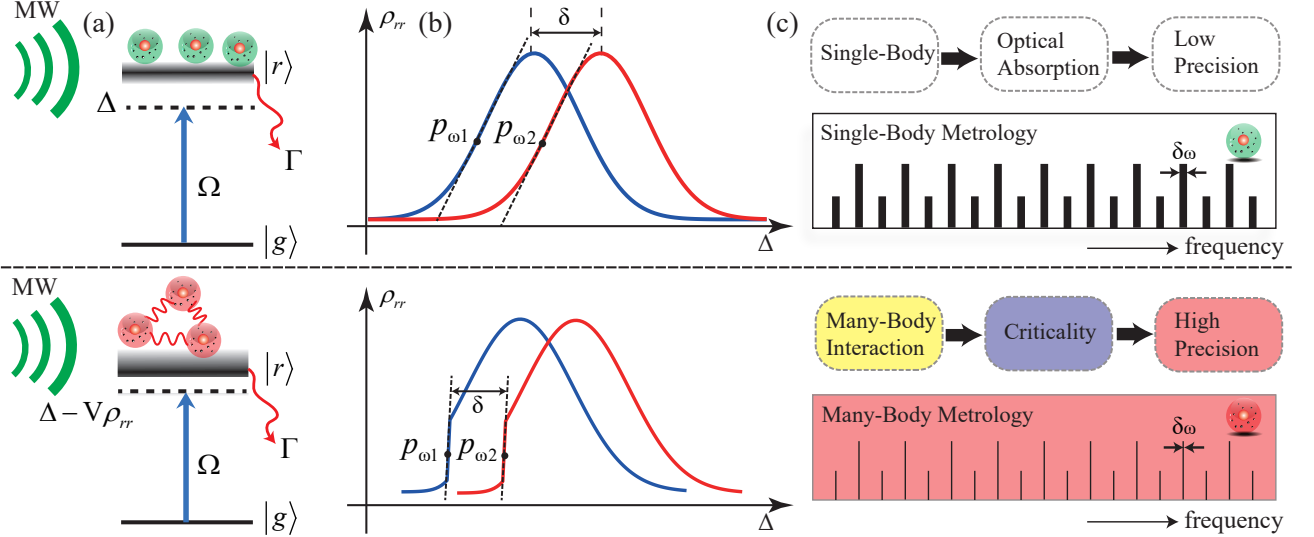


Figure 1. **The principle of single-body [top row] (many-body [bottom row]) Rydberg metrology** (a) Energy diagram for a two-level atom model, showing the ground state $|g\rangle$ and Rydberg state $|r\rangle$ with spontaneous radiation rate, Γ . The atoms are driven from the ground state to the Rydberg state by a laser with Rabi frequency, Ω and detuning, Δ . They are also exposed to a MW field with electric field component E_{mw} . In the many-body case, the Rydberg resonance is modified by the many-body interaction strength, $V = C_6/r^6$ [where C_6 is the van der Waals coefficient and r is the distance between Rydberg atoms], and the population of the Rydberg atoms ρ_{rr} ; see more details in the Method Sections. (b) The blue and red curves represent the spectrum with and without external MW field, which induces a shift δ . The measurement sensitivity is highest when the derivative $d\rho_{rr}/d\Delta$ is maximal, as indicated by the points p_{w1} and p_{w2} . The steeper slope near the critical point in the many-body case [bottom row] results in enhanced measurement sensitivity. (c) The many-body advantage corresponds to a metrological ruler with thinner tick marks $\delta\omega$ than in the single-body case. The transmission spectra are shifted by an external electrical field forming a ruler with unfixed ticks.

state $|g\rangle$ and a Rydberg state $|r\rangle$ (with decay rate Γ) [Fig. 1(a)]. A laser couples these atoms with Rabi frequency Ω and detuning Δ . We derive the Rydberg population ρ_{rr} via mean-field approximation (i.e., $\Delta \rightarrow \Delta - V\rho_{rr}$, where V is the average many-body interaction strength from dipole interaction or ions collisions), δ is the external field induced-frequency shift on Rydberg state $|r\rangle$, as mentioned in Method Sections,

$$\rho_{rr} = \frac{\Omega^2}{4(\Delta - V\rho_{rr})^2 + 2\Omega^2 + \Gamma^2}. \quad (1)$$

Due to the interaction, the spectrum has a population-dependent shift $V\rho_{rr}$, thus inducing a steep edge of ρ_{rr} with a maximum derivative

$$\left. \frac{d\rho_{rr}}{d\Delta} \right|_{\Delta=\Delta_c} = \frac{1}{V + \sqrt{(\Gamma^2 + 2\Omega^2)/3\rho_{rr}^2}}, \quad (2)$$

where Δ_c corresponds to the detuning at which the derivative gets its maximum. We note that the $d\rho_{rr}/d\Delta$ is increased due to the interaction strength V (here $V < 0$); more details can be found in Method Sections. The derivative $d\rho_{rr}/d\Delta$ diverges at the system's critical point [8], exhibiting a method of high-precision measurement [30–36]. A measurement is realized by detecting the transmission of an optical probe field. When applying external fields (such as the electric component of

external microwave MW fields), the measurement precision is limited by the maximum slope of the Rydberg resonance. This is indicated by the points p_{w1} (p_{w2}) in [Fig. 1(b)]. Compared to the non-interacting case [top row], the slope in the vicinity of the critical point [bottom row] is significantly enhanced. For metrology applications, the sensitivity of many-body case is enhanced by a ratio,

$$\beta = \left. \frac{d\rho_{rr}}{d\Delta} \right|_{V \neq 0} / \left. \frac{d\rho_{rr}}{d\Delta} \right|_{V=0}. \quad (3)$$

In Fig. 1(c) we illustrate how this many-body enhancement is like having a new ruler with much finer markings.

The measurement sensitivity is determined by the variation of the transmission signal around the critical point and the photon counting noise in the measurement record. By exploring the linear slope of transmission in a narrow interval around the critical point the sensitivity can be expressed in terms of the Fisher Information [43, 44],

$$F(\Delta) = \frac{\bar{\mu}'(\Delta)^2}{\text{Var}(\mu)} \quad (4)$$

where Δ is the parameter that we want to determine, $\bar{\mu}$ represents the mean value of the difference in photon

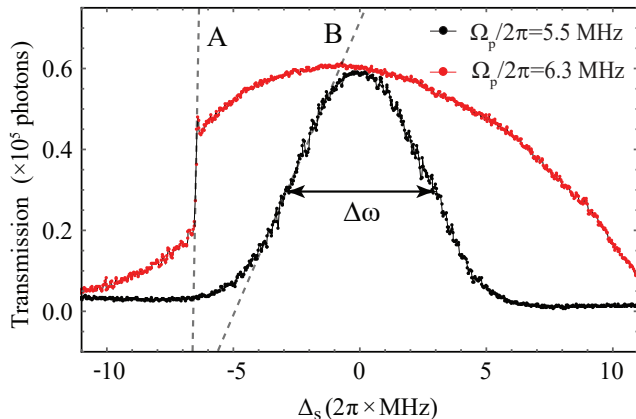


Figure 2. **Optical transmission spectra with and without phase transition.** The transmission spectra with (red) and without (black) phase transition. The dashed lines A and B show the maximum slopes near half transmission. $\Delta\omega/2\pi \sim 6$ MHz shows the bandwidth of the transmission spectrum without interactions. The photon counts are given for a measurement time $t = 20 \mu\text{s}$ for $2\pi \times 0.036$ MHz detuning interval.

numbers accumulated in fixed time intervals by a differential detector exposed to a reference beam and a beam passing through the atomic cloud. $\text{Var}(\mu)$ is the variance of the differential signal, i.e the sum of the variances of the two separate and independent counting signals. Note that Eq.(4) expresses the usual signal-to-noise ratio, and the Cramér-Rao bound,

$$\delta\Delta \geq \frac{1}{\sqrt{F(\Delta)}}. \quad (5)$$

yields the usual estimation error for the counting signal.

It is important to emphasize that the Fisher Information refers to the actual counting signals. While a detector may output a photon rate in counts per second, we must independently assess or estimate the variance of the signal for the time duration of the measurement. We explore experiments with different duration and we shall thus present the actual counts in given time intervals and their variance to obtain the proper assessment of the metrological sensitivity. We shall also observe that during a frequency scan in finite time, the non-interacting (interacting) atomic system does (does not) attain its stationary state. This leads to a linear (non-linear) dependence of the Fisher information on the measurement time.

Measured derivative and Fisher information.

For the experiment, we employ two-photon excitation with a probe beam and a coupling laser beam with Rabi frequencies (detuning) Ω_p (Δ_s) and Ω_c (Δ_c). We measure the transmission spectra, as shown in Fig. 2(a). The transmission depends on Ω_p , and we can prepare the system with and without phase transition $\Omega_p < \Omega_{p,c}$ and $\Omega_p > \Omega_{p,c}$, where $\Omega_{p,c}/2\pi = 5.6$ MHz is the threshold Rabi frequency of the probe field. Our system displays

a second order dynamical phase transition between two stationary states with different excitation densities [21]. The two spectra display the main distinct character of the transmission of a non-interacting system (the black curve in Fig. 2(a)), and an interacting many-body system (the red curve in Fig. 2(a)). The derivative $d\mu/d\Delta_s$ of the transmission is very large at the phase transition point Δ_c of the red curve in Fig. 2(a), while it explores a weaker, finite maximum near half maximum of the black black curve in Fig. 2(a).

In the experiment, we sweep the detuning Δ_s and observe the transmission at each Δ_s . As explained above, the FI is not only governed by the number of excited and thus interacting Rydberg atoms but also depends on the measurement time t [37], defined as the time the probe laser explores a small interval around each detuning Δ_s . In Fig. 3(a-c) we consider the behavior above criticality with $\Omega_p/2\pi = 7.9$ MHz and in Fig. 3(d-f), we consider the behavior below criticality with $\Omega_p/2\pi = 5.5$ MHz. We observe that for $\Omega_p/2\pi = 7.9$ MHz, the transmission profile near the critical point becomes steeper as the measurement time t is increased, while, for $\Omega_p/2\pi = 5.5$ MHz, the transmission spectra are almost identical. This implies that the FI is inclined to be linearly dependent on the time t for the data in Fig. 3(d-f)], while a different dependence appears for the data in Fig. 3(a-c)].

The values of the Fisher Information are shown in Fig. 3(g) for different measurement times t , we find that the FI is fitted well by the form $F = A(t/t_0)^\lambda$, where $A = 2.0 \times 10^4 \text{ MHz}^{-2}$ and $\lambda = 1.28$ for $\Omega_p/2\pi = 7.9$ MHz, while $A = 10 \text{ MHz}^{-2}$ and $\lambda = 1$ for $\Omega_p/2\pi = 5.5$ MHz. In our system, when $t = 1$ ms we achieve a large enhancement ratio up to 10^3 by comparing these two cases. We conclude that one can extract more information by the interacting many-body system than by independent systems, and that we can extract even more information by continuous measurements for long times. The non-integer power-law dependent behavior of the fit to the FI is caused by the critical slowing down and thus deviation of the atomic dynamics from the stationary state around the critical point [45–47]. This smooths the maximum slope and causes a more than linear suppression of the FI for the shorter measurement times in Fig. 3(a-c). We also plot the derivative $d\bar{\mu}/d\Delta_s$ against the detuning Δ_s in the vicinity of the critical detuning at $t = 10\mu\text{s}$, see the inset in Fig. 3(b). We find that the derivative $d\bar{\mu}/d\Delta$ has a power law dependence on detuning $d\bar{\mu}/d\Delta_s = \chi |\Delta_s/\Delta_0 + 11.3|^{-\alpha}$, where $\chi = 0.02 \text{ MHz}^{-1}$, $\Delta_0/2\pi = 1$ MHz, and $\alpha = 2 \pm 0.1$ is the fitted power-law exponent. This detuning-dependent susceptibility is caused by the increased interaction near the critical point [48], as the change of detuning tunes the Rydberg population ρ_{rr} and hence the interaction. For the non-interacting case, the atomic system follows the stationary state even for the fast sweeps in our experiments, and the FI is linearly dependent on time t . There is more noise in Fig. 3 (c) and (f) than Fig. 3 (a) and (d), due to low frequency noises appearing for the longer

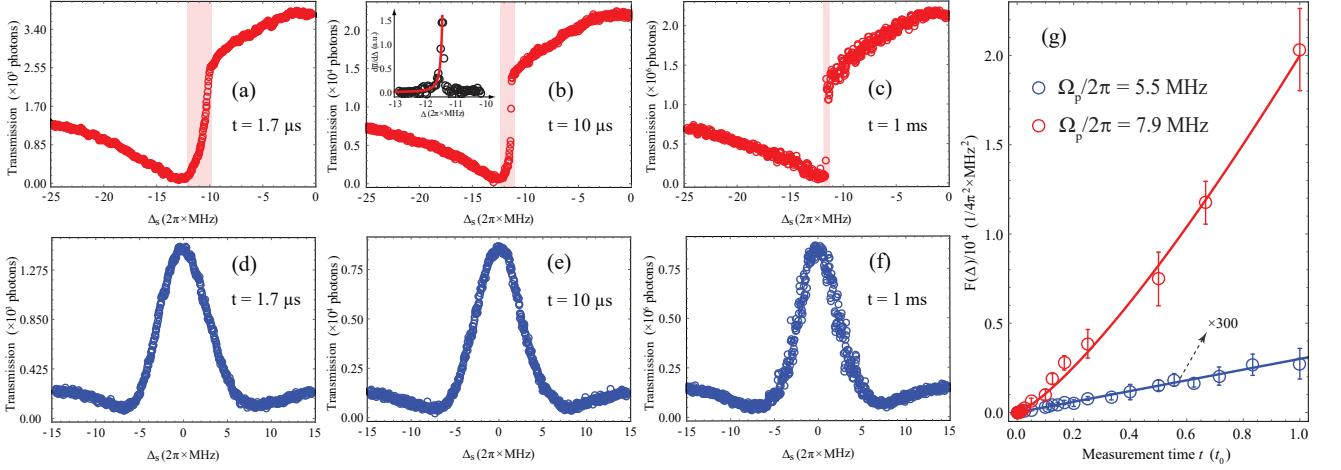


Figure 3. **Transmission spectra and the associated Fisher information.** Panels (a)-(c) show the transmission spectra across the phase transition (shaded regions), obtained in a total measurement time of $t = 1.7 \mu\text{s}$, $t = 10 \mu\text{s}$, and $t = 1 \text{ms}$. The inset in (b) shows the corresponding derivative $d\bar{\mu}/d\Delta_s$. Panels (d)-(f) show the trivial spectra (without phase transition) for the same measurement times $t = 1.7 \mu\text{s}$, $t = 10 \mu\text{s}$, and $t = 1 \text{ms}$. Panel (g) shows the Fisher information associated with the determination of the steepest point on the transmission curves for different values of the total measurement time t (note that the Fisher Information for the non-interacting case is magnified manually by a factor 300). The red and blue curves are fitted by the function $F = A(t/t_0)^\lambda$, where the fit parameters are given in the main text. In this process, the red data in (g) is obtained from the maximum of $F(\Delta)|_{\Delta_s=\Delta_c} = (d\bar{\mu}/d\Delta_s)^2 / \text{Var}(\mu)$, while for the blue data in (g), the FI at the critical point are obtained by considering 30 data points around Δ_c in (d)-(f) to reduce the fluctuations from the instability of the laser power and the cell temperature. The error bars determined in (g) are statistics from the three repeated experiments.

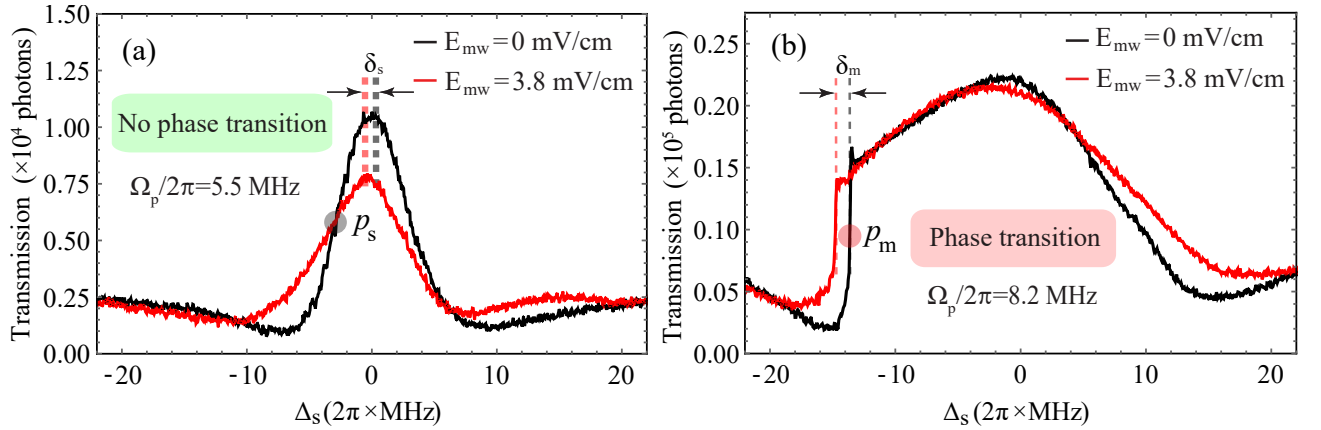


Figure 4. **Change of transmission spectra by application of MW fields.** (a) The transmission spectra under the field amplitude $E_{\text{mw}} = 0 \text{ mV/cm}$ (black) and $E_{\text{mw}} = 3.8 \text{ mV/cm}$ (red) with probe Rabi frequency $\Omega_p = 2\pi \times 5.5 \text{ MHz}$ below the critical value $\Omega_{p,c} = 2$ for the phase transition. (b) The transmission spectra under the field amplitude $E_{\text{mw}} = 0 \text{ mV/cm}$ (black) and $E_{\text{mw}} = 3.8 \text{ mV/cm}$ (red) with the probe Rabi frequency $\Omega_p = 2\pi \times 8.2 \text{ MHz}$, above the critical value for the phase transition. In these two cases, the frequency of the applied MW field is set as $2\pi \times 16.68 \text{ GHz}$. The big circular points p_s and p_m , marked with red and gray in Fig. 4(a) and (b), correspond to the position of the steepest slope. The direction of scanning Δ_c is from the red-detuning towards the blue detuning. Here, Δ_s is swept from $-2\pi \times 30 \text{ MHz}$ to $-2\pi \times 24 \text{ MHz}$ with a sweep rate $v_s = 2\pi \times 0.0055 \text{ MHz}/\mu\text{s}$.

measurement times.

Transmission spectra with and without MW fields. The advantages for metrology appear due to the critical response of the system upon variation of external perturbations. To further study this critical response we apply a MW electric field with amplitude

E_{mw} and detuning Δ_{mw} to continuously drive the Rydberg transition $51D_{3/2} - 52P_{1/2}$. The main effect of the microwave field here is to (1) induce a small AC Stark shift which moves the critical point, (2) change the population of the Rydberg atoms while it has a negligible effect on the C_6 van der Waals coefficient and

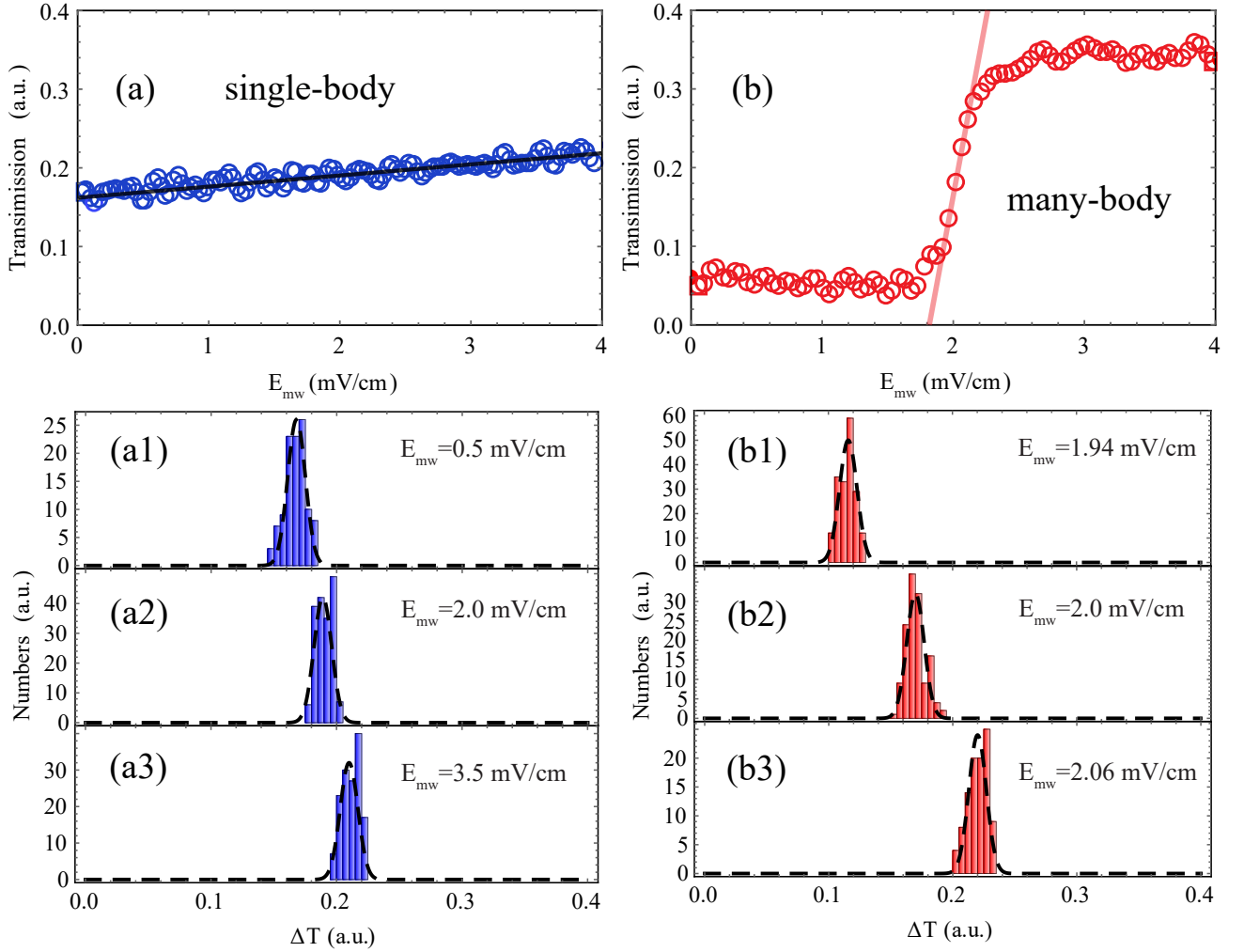


Figure 5. **Transmission under different amplitudes of the MW field for the single-body case (a) and the many-body case (b).** The amplitude E_{mw} is changed from $E_{mw} = 0$ mV/cm to $E_{mw} = 4$ mV/cm in steps of duration $5 \mu\text{s}$. The black and red solid lines are the fit linear functions $y=0.014(x + 11.5)$ and $y=0.89(x - 1.81)$ respectively. (a1-a3) and (b1-b3) are the critical-point histogram of the transmission distribution under the different amplitudes of the MW field with the single-body case and the many-body case, respectively. The dashed lines are fitted Gaussian functions. The data are taken under equivalent experimental conditions (such as scan rate, acquisition time and averaging) in the few- and many-body cases

the resonant dipole-dipole interactions. As shown in Fig. 4(a) and (b), this shifts the transmission spectra of the Rydberg system subject to the probe Rabi frequencies $\Omega_p/2\pi = 5.5$ MHz and $\Omega_p/2\pi = 8.2$ MHz, corresponding to the non-interacting and interacting many-body systems, respectively. When we apply the MW field with $E_{mw} = 3.8$ mV/cm, the spectra show a small red-shift δ_s [Fig. 4(a)] and δ_m [Fig. 4 (b)], respectively. For the many-body system, the high sensitivity of the frequency shift allows us to sense the strength E_{mw} of an applied MW field. The FI $F(\Delta)|_{\Delta_s=\Delta_c}$ for the black data in Fig. 4 (a) is $F = 1.4 \times 10^{-3} \text{MHz}^{-2}$, and is much smaller than that for the black data in Fig. 4 (b) [$F = 0.27 \text{MHz}^{-2}$]. The corresponding minimum uncertainty $\delta\Delta/2\pi \sim 0.3$ MHz corresponds to an uncertainty of the applied field $\Delta E_{mw} = 1.9$ mV/cm by considering the

energy shift proportional to E_{mw}^2 when E_{mw} is small [here the stark shift $\delta_m \sim E_{mw}^2$ follows by a Taylor expansion, $\delta_m \sim -\Delta_{mw}/2 + \sqrt{\Delta_{mw}^2 + \Omega_{mw}^2}/2$], see more data in the supplementary materials. As a result, the many-body system can sense the strength $E_{mw} = 3.8$ mV/cm directly by measuring the spectrum shift [$\delta_m = 2\pi \times 1.2(0.3)$ MHz]. In comparison, the spectral shift δ_s is indistinguishable for independent atoms, which are thus not sensitive enough to sense the same MW field by monitoring of the spectral shift.

Optical response under electric fields with different amplitudes. The many-body metrological ruler has a thinner tick mark and thus a better precision than the single-body ruler, because the optical response is stronger in the many-body case when subject to a small frequency shift. We can also measure the opti-

cal transmission at the position of the steepest slope p_{w1} (Fig. 1(b)) when the atoms are subject to a MW electric field $E_{mw}\sin(f_0t)$ where $f_0/2\pi = 16.60$ GHz is near resonant with the RF transition $51D_{3/2} - 52P_{1/2}$.

We measure the transmission when increasing the amplitude of the MW with the detuning Δ_s fixed near the maximum slope under the many- and single-body conditions, as shown in Fig. 5 (a) and Fig. 5 (b), respectively. For the single-body condition, the transmission is not sensitive to the variance of the amplitude E_{mw} . For the many-body condition, the change of the E_{mw} makes the system cross the critical point and the transmission signal is highly sensitive to the field around values of $E_{mw} = 2$ mV/cm (this position can be tuned by the coupling detuning), as shown in Fig. 5 (b). To evaluate the sensitivity, we fit the data near criticality with a linear function $y = k(x + x_0)$ ($k = \bar{\mu}'(E_{mw})$), and obtain the ratio of the slopes $k_2/k_1 = 63.57$, where k_1 and k_2 represent the linear coefficients for the single- and many-body cases. As the almost same variance $Var(\mu)$ for these two cases, see the following figures (a1-a3) and (b1-b3), we can obtain enhanced ratio for the FI: $(k_2^2/Var(\mu))/(k_1^2/Var(\mu)) > 4000$. From the E_{mw} -dependent transmission, we can distinguish the standard deviation of the amplitude $\delta E_{mw} = 1.4$ mV/cm for the non-interacting case and $\delta E_{mw} = 22$ μ V/cm for the interacting many-body case with 5 μ s data acquisition time per data point. By considering multiple sequential independent measurements, we estimate the equivalent sensitivity 49 nV/cm/Hz^{1/2}.

DISCUSSION

Although the previous work in Ref. [12] clearly shows effects sensitive to the electric field, that work mainly elaborated on how the presence of ionized Rydberg atoms induce a linear shift of the critical point. In contrast, the critical behavior of the interacting many-body system has not previously been employed for sensing. The criticality induced by the interacting Rydberg atoms depends on the Rydberg atom number N and interaction strength V [8], and the increase of the population ρ_{rr} or the interaction strength $V\rho_{rr}$ enhances the non-linearity of the criticality. In our system, we have a large interacting number of atoms, and the energy splitting is far from the one of N isolated systems, cf. previous theoretical works [31–36]. Specifically, the interaction induced non-linear FI dependence on measurement time of a single frequency scan shows a unique advantage on sensing, which agrees with the theoretical simulations in the supplemental materials.

In summary, we have demonstrated the critical behavior of interacting Rydberg atoms and characterised its metrological consequences. The Fisher information for the estimation of a weak microwave field shows an enhancement of order 10^3 by the use of interacting many-body systems. Concerning the use of the Fisher Infor-

mation and Cramér-Rao bound, we note that not only the narrow detuning interval with the highest slope, but the entire transmission signal contributes in an integral manner to the sensitivity of the experiments, cf. a similar analysis of spatial image processing [49, 50]. Our analysis captures the main contribution to that integral and thus constitutes a lower limit to the FI. Passing from the measurement of frequencies, the experiments derive their improved sensitivity towards MW electric fields and show that the Rydberg non-equilibrium system can act as a versatile high-sensitivity metrological resource.

METHOD

Experiment setup. We adopt a two-photon transition scheme to excite an atomic ground-state to a Rydberg-state, using a probe field resonantly driving the atomic transition $5S_{1/2}, F = 2 \rightarrow 5P_{1/2}, F' = 3$, and a coupling field, driving the transition $5P_{1/2}, F' = 3 \rightarrow 51D_{3/2}$. An MW electric field 1 (or 2) may be applied to drive an RF transition between two different Rydberg states $51D_{3/2}$ and $52P_{1/2}$ (or $50F_{5/2}$). The MW electric fields used in our experiment are generated by two RF sources and two frequency horns. A 795 nm laser is split by a beam displacer into a probe beam and an identical reference beam, which are both propagating in parallel through a heated Rb cell (length 10 cm). The temperature is set as 44.6°C, corresponding to the atomic density of 9.0×10^{10} cm⁻³. One probe beam is overlapped with a counter-propagating coupling beam to constitute the Rydberg-EIT process. The two transmission signals are detected on a differencing photodetector.

Generation and calibration of MW fields. The MW fields used in our experiment are generated by two RF sources and two frequency horns. The RF source 1 works in the range from DC to 40 GHz, another is in the range from DC to 20 GHz. The frequency horns are set close to the Rb cell. The RF frequency between Rydberg D and P/F states are calculated according to the algorithm in Ref. [51]. We use a spectrum analyzer (Ceyear 4024F, 9 kHz \sim 32 GHz) and an antenna (380 MHz \sim 20 GHz) to receive the MW fields then to calibrate the amplitude of MW fields in the centre of the Rb cell.

Fisher information and Cramér-Rao bound. In parameter estimation, the Cramér-Rao bound sets a lower limit to the statistical estimation error by ν independent experiments, $(\delta\theta)_{min} = 1/\sqrt{\nu \cdot F(\theta)}$. Here $F(\theta)$ is the Fisher Information (FI) which has the value

$$F(\theta) = \sum_{\mu} \frac{1}{L(\mu, \theta)} \left(\frac{\partial L(\mu, \theta)}{\partial \theta} \right)^2, \quad (6)$$

where $L(\mu, \theta)$ is the likelihood function for the possible measurement outcome μ , conditioned on the parameter θ [52]. In our experiment we subtract two counting signals which may both be well described by Poisson distributions with mean values $\bar{\mu}_1$ and $\bar{\mu}_2$, and the same values

for their variances. Both count numbers are large, and in our experiments the observed noise is dominated by electronic noise, and hence the distributions are both well approximated by Gaussian distributions. The difference signal is thus described by a Gaussian distribution with mean value $\bar{\mu} = \bar{\mu}_1 - \bar{\mu}_2$ and variance $\sigma^2 = \bar{\mu}_1 + \bar{\mu}_2$. For a Gaussian distribution with the likelihood [53, 54]

$$L(\mu, \theta) = \frac{1}{\sqrt{2\pi\sigma^2}} e^{-\frac{1}{2}\left(\frac{\mu - \bar{\mu}(\theta)}{\sigma}\right)^2} \quad (7)$$

one can see that

$$\frac{\partial L(\mu, \theta)}{\partial \theta} = \left(\frac{\mu - \bar{\mu}}{\sigma^2}\right) L(\mu, \theta) \bar{\mu}'(\theta). \quad (8)$$

We hence obtain

$$\begin{aligned} F(\theta) &= \sum_{\mu} \frac{1}{L(\mu, \theta)} \left(\left(\frac{\mu - \bar{\mu}}{\sigma^2} \right) L(\mu, \theta) \bar{\mu}'(\theta) \right)^2 \\ &= \sum_{\mu} L(\mu, \theta) \frac{(\mu - \bar{\mu})^2}{\sigma^4} (\bar{\mu}'(\theta))^2 \\ &= \frac{Var(\mu)}{\sigma^4} (\bar{\mu}'(\theta))^2 = \frac{(\bar{\mu}'(\theta))^2}{\sigma^2} \end{aligned} \quad (9)$$

where $\bar{\mu}'(\theta)$ denotes the derivative of the mean $\bar{\mu}(\theta)$ w.r.t θ . There is a further contribution to the FI due to the dependence of the variance σ^2 on θ . Its value is $\frac{1}{2\sigma^4} \left(\frac{d(\sigma^2)}{d\theta} \right)^2$, and for our system it plays a less important role.

Signal to ratio analysis. For a given Gaussian incident probe and reference beams with mean photon signal μ_0 in one second, the on-resonance absorption coefficient of the atoms and the loss of the optical path is $1 - \zeta$ (corresponding to the transmission ratio ζ), a differencing photodetector with efficiency η , records a Poisson distributed number of clicks with mean value $\eta\mu_0$ and variance $\eta\mu_0$ per second, which outputs a voltage signal. The difference between two beams is much weaker and has the mean value

$$\mu = \zeta\eta\mu_0[1 + \varepsilon(\Delta_s)]t - \zeta\eta\mu_0 t = \zeta\eta\mu_0\varepsilon(\Delta_s)t \quad (10)$$

where $\varepsilon(\Delta_s)$ is the transmission probability induced by Rydberg-EIT effect, t is the considered time interval. As the input photon number of each beam is very large $\mu_0 \sim 10^{14}$ photons per second for $\Omega_p/2\pi = 7.9$ MHz, the variance of the difference of the two beams per second is the sum of the means because the difference of two Gaussian-distributed variables is also a Gaussian distributed variable: $Var(\mu) = 2\zeta\eta\mu_0 + \zeta\eta\mu_0\varepsilon(\Delta_s) \sim 2\zeta\eta\mu_0$. $\zeta = 20.6\%$ for $\Omega_p/2\pi = 7.9$ MHz, $\zeta = 14.6\%$ for $\Omega_p/2\pi = 6.5$ MHz, $\zeta = 8.7\%$ for $\Omega_p/2\pi = 5.5$ MHz. The output voltage signal of the differencing photodetector could be converted into the photon number by a voltage conversion ratio $G = 5.3 \times 10^7$ V/W. The 0.5 voltage output signal corresponds to $\sim 1 \times 10^{10}$ photon numbers per second. The coupling detuning Δ_s is swept with a rate of v_s

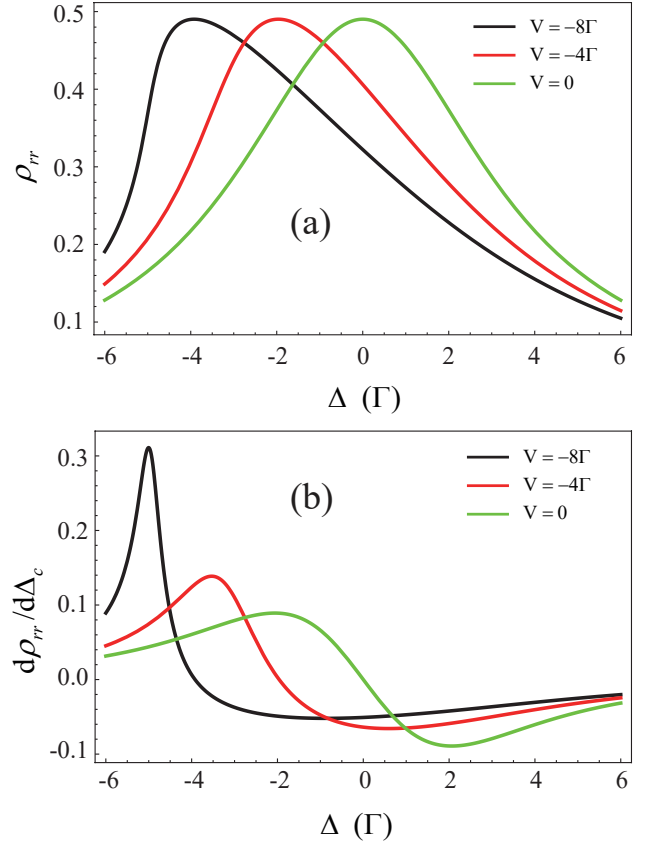


Figure 6. **Theoretical simulations of interacting two-level atoms.** (a) Rydberg state population ρ_{rr} as a function of laser detuning Δ for different interaction strengths V . (b) The derivative of Rydberg population with respect to Δ .

and with M sampling rate [means that there are average M data points in the swept detuning Δ_s], the transmission spectrum could be measured by accumulating the photon numbers in each detuning interval. The fast scan accumulate small photon numbers for each interval, while the slow scan get large photon numbers. If we scan the detuning of coupling laser Δ_s from red- to blue-detuning and vice versa, we could observe the bistability, see also in Refs. [7, 8, 55]. The bistability shifted by the MW fields could be found in the supplementary materials.

Non-linearity of interacting atoms. To elucidate the sensitivity of the Rydberg atoms to the frequency for different interaction strength, we consider a two-level atoms model with ground state $|g\rangle$ and Rydberg state $|r\rangle$ (with spontaneous radiation rate Γ), which are coupled by a laser with Rabi frequency Ω and detuning from resonance Δ . After mean-field approximation (i.e., $\Delta \rightarrow \Delta - V\rho_{rr}$, where V is the many-body interaction term from dipole interaction or ions collisions, and ρ_{rr} is the population of the Rydberg state), the steady-state solution for a two-level optical Bloch equation is [20]

$$\begin{aligned} \dot{\rho}_{gr} &= i\frac{\Omega}{2}(\rho_{rr} - \rho_{gg}) + i\Delta_{\text{eff}}\rho_{gr} - \frac{\Gamma}{2}\rho_{gr} \\ \dot{\rho}_{rr} &= -i\Omega(\rho_{gr} - \rho_{rg}) - \Gamma\rho_{rr} \end{aligned} \quad (11)$$

where Δ_{eff} is the effective detuning $\Delta_{\text{eff}} = \Delta - V\rho_{rr}$ by considering an interaction strength V . We obtain an equation about ρ_{rr} for bistability as follows

$$V^2\rho_{rr}^3 - 2V\Delta\rho_{rr}^2 + (\Delta^2 + \Omega^2/2 + \Gamma^2/4)\rho_{rr} - \Omega^2/4 = 0 \quad (12)$$

By taking the derivative of both sides, we finally get the relationship between the slope of the steep edge of the hysteresis loop $\max(d\rho_{rr}/d\Delta)$ and the interaction of Rydberg atoms V .

$$\frac{d\rho_{rr}}{d\Delta} = -\frac{8(\Delta\rho_{rr} - \rho_{rr}^2V)}{\Gamma^2 + 4\Delta^2 + 12\rho_{rr}^2V^2 - 16\Delta\rho_{rr}V + 2\Omega^2} \quad (13)$$

The critical point is defined when this derivative reaches infinity $d\rho_{rr}/d\Delta \Rightarrow \infty$, from which the threshold of the Rydberg population is obtained, i.e.,

$$\rho_{th} = \frac{\sqrt{-3\Gamma^2V^2 + 4\Delta^2V^2 - 6V^2\Omega^2} + 4\Delta V}{6V^2}. \quad (14)$$

The relation between ρ_{rr} , $d\rho_{rr}/d\Delta$, and Δ is demonstrated in Fig. 6. And by letting the derivative equals to 0, i.e., $d\rho_{rr}/d\Delta = 0$, we obtain the analytical expression of maximum derivative $d\rho_{rr}/d\Delta|_{\Delta=\Delta_c}$ and the corresponding detuning Δ_c as follows

$$\Delta_c = \frac{1}{6} \left(6\rho_{rr}V - \sqrt{3}\sqrt{\Gamma^2 + 2\Omega^2} \right) \quad (15)$$

$$\frac{d\rho_{rr}}{d\Delta}(\Delta_c) = \frac{1}{V + \sqrt{(\Gamma^2 + 2\Omega^2)/3\rho_{rr}^2}} \quad (16)$$

Data availability. The data that support this study are available at Github [56] ([many-body-enhanced-metrology](#)).

-
- [1] M. Greiner, O. Mandel, T. Esslinger, T. W. Hänsch, and I. Bloch, Quantum phase transition from a superfluid to a mott insulator in a gas of ultracold atoms, *Nature* **415**, 39 (2002).
- [2] H. Bernien, S. Schwartz, A. Keesling, H. Levine, A. Omran, H. Pichler, S. Choi, A. S. Zibrov, M. Endres, M. Greiner, *et al.*, Simulating many-body dynamics on a 51-atom quantum simulator, *Nature* **551**, 579 (2017).
- [3] M. J. Martin, M. Bishof, M. D. Swallows, X. Zhang, C. Benko, J. von Stecher, A. V. Gorshkov, A. M. Rey, and J. Ye, A quantum many-body spin system in an optical lattice clock, *Science* **341**, 632 (2013).
- [4] S. Colombo, E. Pedrozo-Peñañafel, A. F. Adiyatullin, Z. Li, E. Mendez, C. Shu, and V. Vuletic, Time-reversal-based quantum metrology with many-body entangled states, *arXiv: 2106.03754* (2021).
- [5] M. D. Lukin, M. Fleischhauer, R. Cote, L. M. Duan, D. Jaksch, J. I. Cirac, and P. Zoller, Dipole blockade and quantum information processing in mesoscopic atomic ensembles, *Phys. Rev. Lett.* **87**, 037901 (2001).
- [6] M. Saffman, T. G. Walker, and K. Mølmer, Quantum information with Rydberg atoms, *Rev. Mod. Phys.* **82**, 2313 (2010).
- [7] C. Carr, R. Ritter, C. Wade, C. S. Adams, and K. J. Weatherill, Nonequilibrium phase transition in a dilute Rydberg ensemble, *Phys. Rev. Lett.* **111**, 113901 (2013).
- [8] D.-S. Ding, H. Busche, B.-S. Shi, G.-C. Guo, and C. S. Adams, Phase diagram of non-equilibrium phase transition in a strongly-interacting Rydberg atom vapour, *Phys. Rev. X* **10**, 021023 (2020).
- [9] N. Malossi, M. Valado, S. Scotto, P. Huillery, P. Pillet, D. Ciampini, E. Arimondo, and O. Morsch, Full counting statistics and phase diagram of a dissipative Rydberg gas, *Phys. Rev. Lett.* **113**, 023006 (2014).
- [10] N. R. de Melo, C. G. Wade, N. Šibalić, J. M. Kondo, C. S. Adams, and K. J. Weatherill, Intrinsic optical bistability in a strongly driven Rydberg ensemble, *Phys. Rev. A* **93**, 063863 (2016).
- [11] N. Šibalić, C. G. Wade, C. S. Adams, K. J. Weatherill, and T. Pohl, Driven-dissipative many-body systems with mixed power-law interactions: Bistabilities and temperature-driven nonequilibrium phase transitions, *Phys. Rev. A* **94**, 011401 (2016).
- [12] C. G. Wade, M. Marcuzzi, E. Levi, J. M. Kondo, I. Lesanovsky, C. S. Adams, and K. J. Weatherill, A terahertz-driven non-equilibrium phase transition in a room temperature atomic vapour, *Nature Communications* **9**, 1 (2018).
- [13] T. Wintermantel, M. Buchhold, S. Shevate, M. Morgado, Y. Wang, G. Lochead, S. Diehl, and S. Whitlock, Epidemic growth and griffiths effects on an emergent network of excited atoms, *Nature Communications* **12**, 1 (2020).
- [14] D.-S. Ding, Z.-K. Liu, H. Busche, B.-S. Shi, G.-C. Guo, C. S. Adams, and F. Nori, Epidemic spreading and herd immunity in a driven non-equilibrium system of strongly-interacting atoms, *arXiv: 2106.12290* (2021).
- [15] H. Gibbs, S. McCall, and T. Venkatesan, Differential gain and bistability using a sodium-filled fabry-perot interferometer, *Phys. Rev. Lett.* **36**, 1135 (1976).
- [16] H. Wang, D. Goorskey, and M. Xiao, Bistability and instability of three-level atoms inside an optical cavity, *Phys. Rev. A* **65**, 011801 (2001).
- [17] H. Wang, D. Goorskey, and M. Xiao, Enhanced kerr non-linearity via atomic coherence in a three-level atomic system, *Phys. Rev. Lett.* **87**, 073601 (2001).
- [18] L. Pickup, K. Kalinin, A. Askitopoulos, Z. Hatzopoulos, P. Savvidis, N. G. Berloff, and P. Lagoudakis, Optical bistability under nonresonant excitation in spinor polariton condensates, *Phys. Rev. Lett.* **120**, 225301 (2018).
- [19] M. Hehlen, H. Güdel, Q. Shu, J. Rai, S. Rai, and S. Rand, Cooperative bistability in dense, excited atomic systems, *Phys. Rev. Lett.* **73**, 1103 (1994).
- [20] T. E. Lee, H. Haeffner, and M. Cross, Collective quantum jumps of Rydberg atoms, *Phys. Rev. Lett.* **108**, 023602 (2012).
- [21] M. Marcuzzi, E. Levi, S. Diehl, J. P. Garrahan, and

- I. Lesanovsky, Universal nonequilibrium properties of dissipative Rydberg gases, *Phys. Rev. Lett.* **113**, 210401 (2014).
- [22] H. Weimer, Variational principle for steady states of dissipative quantum many-body systems, *Phys. Rev. Lett.* **114**, 040402 (2015).
- [23] E. Levi, R. Gutiérrez, and I. Lesanovsky, Quantum nonequilibrium dynamics of Rydberg gases in the presence of dephasing noise of different strengths, *Journal of Physics B* **49**, 184003 (2016).
- [24] H. Fan, S. Kumar, J. Sedlacek, H. Kübler, S. Karimkashi, and J. P. Shaffer, Atom based rf electric field sensing, *Journal of Physics B* **48**, 202001 (2015).
- [25] J. A. Sedlacek, A. Schwettmann, H. Kübler, R. Löw, T. Pfau, and J. P. Shaffer, Microwave electrometry with Rydberg atoms in a vapour cell using bright atomic resonances, *Nature Physics* **8**, 819 (2012).
- [26] A. Facon, E.-K. Dietsche, D. Grosso, S. Haroche, J.-M. Raimond, M. Brune, and S. Gleyzes, A sensitive electrometer based on a Rydberg atom in a schrödinger-cat state, *Nature* **535**, 262 (2016).
- [27] K. C. Cox, D. H. Meyer, F. K. Fatemi, and P. D. Kunz, Quantum-limited atomic receiver in the electrically small regime, *Phys. Rev. Lett.* **121**, 110502 (2018).
- [28] M. Jing, Y. Hu, J. Ma, H. Zhang, L. Zhang, L. Xiao, and S. Jia, Atomic superheterodyne receiver based on microwave-dressed Rydberg spectroscopy, *Nature Physics* **16**, 911 (2020).
- [29] Z.-K. Liu, L.-H. Zhang, B. Liu, Z.-Y. Zhang, G.-C. Guo, D.-S. Ding, and B.-S. Shi, Deep learning enhanced Rydberg multifrequency microwave recognition, *Nature Communications* **13**, <https://doi.org/10.1038/s41467-022-29686-7> (2022).
- [30] S. Gammelmark and K. Mølmer, Phase transitions and heisenberg limited metrology in an ising chain interacting with a single-mode cavity field, *New Journal of Physics* **13**, 053035 (2011).
- [31] K. Macieszczak, M. Guță, I. Lesanovsky, and J. P. Garrahan, Dynamical phase transitions as a resource for quantum enhanced metrology, *Phys. Rev. A* **93**, 022103 (2016).
- [32] S. Fernández-Lorenzo and D. Porras, Quantum sensing close to a dissipative phase transition: Symmetry breaking and criticality as metrological resources, *Phys. Rev. A* **96**, 013817 (2017).
- [33] M. Raghunandan, J. Wrachtrup, and H. Weimer, High-density quantum sensing with dissipative first order transitions, *Phys. Rev. Lett.* **120**, 150501 (2018).
- [34] L. Garbe, M. Bina, A. Keller, M. G. A. Paris, and S. Felicetti, Critical quantum metrology with a finite-component quantum phase transition, *Phys. Rev. Lett.* **124**, 120504 (2020).
- [35] Y. Chu, S. Zhang, B. Yu, and J. Cai, Dynamic framework for criticality-enhanced quantum sensing, *Phys. Rev. Lett.* **126**, 010502 (2021).
- [36] V. Montenegro, U. Mishra, and A. Bayat, Global sensing and its impact for quantum many-body probes with criticality, *Phys. Rev. Lett.* **126**, 200501 (2021).
- [37] T. Ilias, D. Yang, S. F. Huelga, and M. B. Plenio, Criticality enhanced quantum sensing via continuous measurement, *arXiv preprint arXiv:2108.06349* (2021).
- [38] L. Garbe, O. Abah, S. Felicetti, and R. Puebla, Critical quantum metrology with fully-connected models: From heisenberg to kibble-zurek scaling, *arXiv preprint arXiv:2110.04144* (2021).
- [39] R. Liu, Y. Chen, M. Jiang, X. Yang, Z. Wu, Y. Li, H. Yuan, X. Peng, and J. Du, Experimental critical quantum metrology with the heisenberg scaling, *npj Quantum Information* **7**, 1 (2021).
- [40] P. Zanardi, M. G. A. Paris, and L. Campos Venuti, Quantum criticality as a resource for quantum estimation, *Phys. Rev. A* **78**, 042105 (2008).
- [41] D. Rossini and E. Vicari, Dynamic kibble-zurek scaling framework for open dissipative many-body systems crossing quantum transitions, *Physical Review Research* **2**, 023211 (2020).
- [42] A. Pelissetto, D. Rossini, and E. Vicari, Dynamic finite-size scaling after a quench at quantum transitions, *Physical Review E* **97**, 052148 (2018).
- [43] L. Pezzè, A. Smerzi, M. K. Oberthaler, R. Schmied, and P. Treutlein, Quantum metrology with nonclassical states of atomic ensembles, *Rev. Mod. Phys.* **90**, 035005 (2018).
- [44] S. L. Braunstein, C. M. Caves, and G. J. Milburn, Generalized uncertainty relations: theory, examples, and lorentz invariance, *Annals of physics* **247**, 135 (1996).
- [45] W. H. Zurek, U. Dorner, and P. Zoller, Dynamics of a quantum phase transition, *Phys. Rev. Lett.* **95**, 105701 (2005).
- [46] L. W. Clark, L. Feng, and C. Chin, Universal space-time scaling symmetry in the dynamics of bosons across a quantum phase transition, *Science* **354**, 606 (2016).
- [47] A. Keesling, A. Omran, H. Levine, H. Bernien, H. Pichler, S. Choi, R. Samajdar, S. Schwartz, P. Silvi, S. Sachdev, *et al.*, Quantum kibble-zurek mechanism and critical dynamics on a programmable Rydberg simulator, *Nature* **568**, 207 (2019).
- [48] A. Trenkwalder, G. Spagnolli, G. Semeghini, S. Coop, M. Landini, P. Castilho, L. Pezzè, G. Modugno, M. Inguscio, A. Smerzi, and *et al.*, Quantum phase transitions with parity-symmetry breaking and hysteresis, *Nature Physics* **12**, 826–829 (2016).
- [49] A. Negretti, C. Henkel, and K. Mølmer, Quantum-limited position measurements of a dark matter-wave soliton, *Physical Review A* **77**, [10.1103/physrevA.77.043606](https://doi.org/10.1103/physrevA.77.043606) (2008).
- [50] V. Delaubert, N. Treps, C. Fabre, H. A. Bachor, and P. Réfrégier, Quantum limits in image processing, *EPL (Europhysics Letters)* **81**, 44001 (2008).
- [51] N. Šibalić, J. D. Pritchard, C. S. Adams, and K. J. Weatherill, Arc: An open-source library for calculating properties of alkali Rydberg atoms, *Computer Physics Communications* **220**, 319 (2017).
- [52] E. L. Lehmann and G. Casella, *Theory of Point Estimation* (Springer, New York, 1998).
- [53] K. V. Mardia and R. J. Marshall, Maximum likelihood estimation of models for residual covariance in spatial regression, *Biometrika* **71**, 135 (1984).
- [54] K. S. Miller, *Complex stochastic processes: an introduction to theory and application* (Addison Wesley Publishing Company, 1974).
- [55] D. Weller, A. Urvoy, A. Rico, R. Löw, and H. Kübler, Charge-induced optical bistability in thermal Rydberg vapor, *Phys. Rev. A* **94**, 063820 (2016).
- [56] Z.-K. Liu, *Zongkailiu/many-body-enhanced-metrology*: (2022).

Acknowledgment. D-S.D thanks for discussions with professor Jun Ye from JILA. Z-K.L. appreciates

instructive discussions with Dr. Tian-Yu Xie. We acknowledge funding from National Key Research and Development Program of China (2017YFA0304800), the National Natural Science Foundation of China (Grant Nos. U20A20218, 61525504, 61722510, 61435011), the Innovation Program for Quantum Science and Technology (2021ZD0301100), Anhui Initiative in Quantum Information Technologies (AHY020200), the Youth Innovation Promotion Association of Chinese Academy of Sciences under Grant No. 2018490, EPSRC through grant agreements EP/M014398/1 (“Rydberg soft matter”), EP/R002061/1 (“Atom-based Quantum Photonics”), EP/L023024/1 (“Cooperative quantum optics in dense thermal vapours”), EP/P012000/1 (“Solid State Superatoms”), EP/R035482/1 (“Optical Clock Arrays

for Quantum Metrology”), EP/S015973/1 (“Microwave and Terahertz Field Sensing and Imaging using Rydberg Atoms”), the Danish National Research Foundation through the Center of Excellence for Complex Quantum Systems (Grant agreement No. DNRF156), as well as, DSTL, and Durham University.).

Author contributions. D-S.D. conceived the idea and implemented the physical experiments with Z-K.L. Z-K.L., D-S.D., and K.M. employ the Fisher information. D-S.D., Z-K.L., and K.M. derived the equations, plotted figures, and wrote the manuscript. All authors contributed to discussions regarding the results and analysis contained in the manuscript. D-S.D., B-S.S., G-C.G., K.M., and C-S.A. support this project.

Competing interests. The authors declare no competing interests.

Supplementary materials of enhanced metrology at the critical point of a many-body Rydberg atomic system

Dong-Sheng Ding^{1,2,3,*,\dagger}, Zong-Kai Liu^{1,2,3,*}, Bao-Sen Shi^{1,2,3,\ddagger},
Guang-Can Guo^{1,2,3}, Klaus Mølmer^{4,\S}, and Charles S. Adams^{5,\P}

¹CAS Key Laboratory of Quantum Information, University of Science and Technology of China, Hefei 230026, China

²CAS Center for Excellence in Quantum Information and Quantum Physics,
University of Science and Technology of China, Hefei 230026, China

³Hefei National Laboratory, University of Science and Technology of China, Hefei 230088, China

⁴Aarhus Institute of Advanced Studies, Aarhus University,
Høegh-Guldbergs Gade 6B, DK-8000 Aarhus C, Denmark
Center for Complex Quantum Systems, Department of Physics and Astronomy,
Aarhus University, Ny Munkegade 120, DK-8000 Aarhus C, Denmark and

⁵Department of Physics, Durham University, South Road, Durham DH1 3LE, United Kingdom

(Dated: July 28, 2022)

Simulation on the time-dependent dynamics. In order to analyze the dynamics at the criticality, we simulate the dynamics of the Rydberg population ρ_{rr} under different measurement time t by changing the sweep rate. By considering the time-dependent terms $\dot{\rho}_{gr}$ and $\dot{\rho}_{rr}$ in the equation (7) in main text, we solve the transient solution and obtain the Rydberg population ρ_{rr} at different evolution time t for each detuning Δ , here the evolution time is equivalent to the time required for measurement. In this process, the sampling rates are 400, it means there are 400 data points in the average distribution from $-2\pi \times 40$ MHz $\sim 2\pi \times 40$ MHz. For the interaction $V/2\pi = -35$ MHz, the derivative $d\rho_{rr}/d\Delta$ at the critical detuning decreases against the measurement time t , see the results in Figs. S1(a-c). For $t = \tau, 2\tau$ and 10τ , when $V/2\pi = -35$ MHz, we obtain $d\rho_{rr}/d\Delta = 0.22, 0.52$, and 0.83 respectively. While for $V = 0$, the derivative $d\rho_{rr}/d\Delta = 0.03$ at the steepest position, with no obvious change for different measurement time t . From these results, the derivative $d\rho_{rr}/d\Delta$ for the interacted many-body system has an obvious scale-up on the time t by comparing that in the independent single-body system.

According to the mean field model, we have calculated the Fisher information $F(\Delta)|_{\Delta=\Delta_c} = (d\bar{\mu}/d\Delta)^2/\sigma^2$ for the interacted many-body system [$V/2\pi = -35, -30, -28$ MHz] and independent single-body system [$V/2\pi = 0$ MHz], which are given by the red and blue data of the Fig. S1(g). For the many-body case, there is a nonlinear dependence of the Fisher information with data acquisition time, while for the single-body case, the Fisher information increases linearly with time t . The nonlinear feature of the Fisher information is also dependent on the interaction strength V . The larger the interaction strength V , the larger is the exponent λ .

Double MW shifted bistability. In our experiment, the different scan directions give rise to hysteresis characterizing as the optical bistability. Due to the high-precision of the criticality on detuning, the bistability shift could be measured in small variance. We have studied the cases with two different MW electric fields $f_{MW1} = 2\pi \times 16.60$ GHz and $f_{MW2} = 2\pi \times 17.20$ GHz experimentally, both of these are under the red-detuning case. We first measure the bistability without the MW electric fields shown in Fig. S2(a), and then open on the MW electric fields 1 and 2 individually, as given in Fig. S2(c) and Fig. S2(e). The bistability has a blue-shift of $2\pi \times 3.7$ MHz for the MW electric field 1, and a red-shift of $-2\pi \times 5.8$ MHz for the MW electric field 2. The reason why the different shift directions of the bistability for the states $52P_{1/2}$ and $50F_{5/2}$ is that the $52P_{1/2}$ state is lower (lambda-type energy diagram with $51D_{3/2}$ and $5P_{1/2}$) and the $50F_{5/2}$ state higher (ladder-type energy diagram with $51D_{3/2}$ and $5P_{1/2}$) in energy than the $51D_{3/2}$ state. The detuning Δ_{mw} is thus opposite for upper and lower Rydberg states. The double jumps in the hysteresis loop result in double FI peaks, as marked as red and black color in Fig. S2(b), (d) and (f). The FI in the right-left scanning case [red in Fig. S2(b), (d) and (f)] is smaller than that in the left-right scanning case [black in Fig. S2(b), (d) and (f)]. This is because the bifurcation of many-body system at small detuning is more distinct than that at large detuning [1]. For any given swept experiment, there is high-sensitivity criticality for frequency shift under Δ_s goes up [black in Fig. S2(b), (d) and (f)] or drop down [red in Fig. S2(b), (d) and (f)].

Measurement of the shifted critical point. We measure the frequency shift of the transition point [or the maximum FI] for these two cases, as shown in Fig. S3(a). If tuning the shift with multiple MW electric fields, we could change the shift in back and forth by multiple MW electric fields. To demonstrate this effect, we record the transmission spectra with the MW electric fields 1 and 2 both off (black), the MW electric fields 1 off and 2 on (blue), and the MW electric fields 1 and 2 both on

* These authors contributed equally to this work.

^{\dagger} dds@ustc.edu.cn

^{\ddagger} drshi@ustc.edu.cn

^{\S} moelmer@phys.au.dk

^{\P} c.s.adams@durham.ac.uk

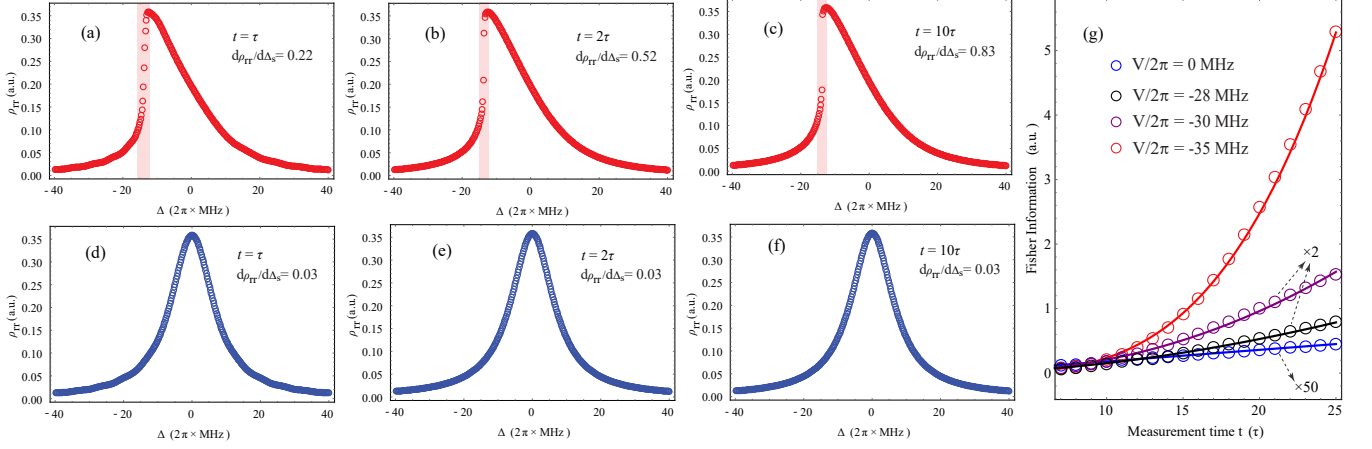


Figure S1. **Simulation on transmission dynamics of single- and many-body system.** The simulated population ρ_{rr} against different sweep rates (or measurement time t) under the interaction strength $V/2\pi = -35$ MHz for (a-c) and $V = 0$ MHz for (d-f). In this simulation, $\Gamma/2\pi = 8$ MHz and $\Omega/2\pi = 9$ MHz. (g) The calculated Fisher information $F(\Delta)|_{\Delta=\Delta_c} = (d\bar{\mu}/d\Delta)^2/\bar{\mu}$ under $V/2\pi = -35$ MHz (red), $V/2\pi = -30$ MHz (purple), $V/2\pi = -28$ MHz (black), and $V/2\pi = 0$ MHz (blue), here $\bar{\mu} = \int \rho_{rr} dt$. The theoretical fit function for these two cases is $F = At^\lambda$, where $A = 9.3 \times 10^{-5}$ MHz $^{-2}$ and $\lambda = 3.4$ for $V/2\pi = -35$ MHz, $A = 1.3 \times 10^{-3}$ MHz $^{-2}$ and $\lambda = 2.2$ for $V/2\pi = -30$ MHz, $A = 2.6 \times 10^{-3}$ MHz $^{-2}$ and $\lambda = 1.78$ for $V/2\pi = -28$ MHz, and $A = 3.6 \times 10^{-4}$ MHz $^{-2}$ and $\lambda = 1$ for $V/2\pi = 0$ MHz. The Fisher Information for the blue, black, and purple data are magnified manually by a factor 50, 2, and 2 respectively.

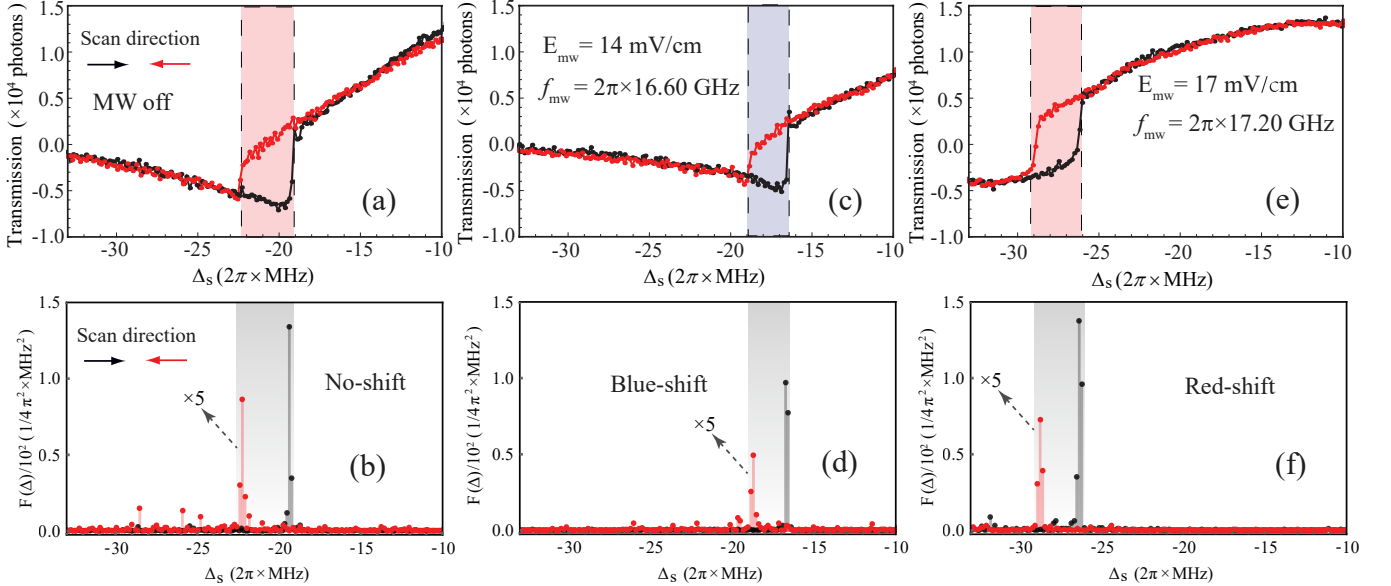


Figure S2. **Microwave electric fields shifted bistability.** The measured bistability without any MW electric field (a), with the MW electric field 1 (c), and with the MW electric field 2 (e). The bistability regions, as marked by the shaded areas in (c) and (e), show an obvious frequency shift by comparing with (a). In these cases, the intensity of the MW electric fields is set as $E_{mw1} = 14$ mV/cm and $E_{mw2} = 17$ mV/cm. The corresponding Fisher information distributions with no-shift, blue-shift and, red-shift are given in (b), (d), and (f). The label $\times 5$ of red dots means that the Fisher information of the right-left scanning case is magnified manually by 5 times for better illustration. The shaded areas represent the width between the maximum Fisher information by scanning Δ_s with two different directions.

(red), as shown in Fig. S3(b). Without the MW electric fields, the phase transition appears at $-2\pi \times 20.2$ MHz. If applying the MW electric field 2, the phase transition point is shifted to $-2\pi \times 22.6$ MHz, but shifted back to $-2\pi \times 21.4$ MHz when the MW electric field 1 is on. These

show that the criticality of phase transition is red-shifted by the MW electric field 2, and then could be shifted back a little bit due to the opposite shifts for $52P_{1/2}$ and $50F_{5/2}$. When increasing E_{mw} , the phase transition is inclined to disappear because the Rydberg populations

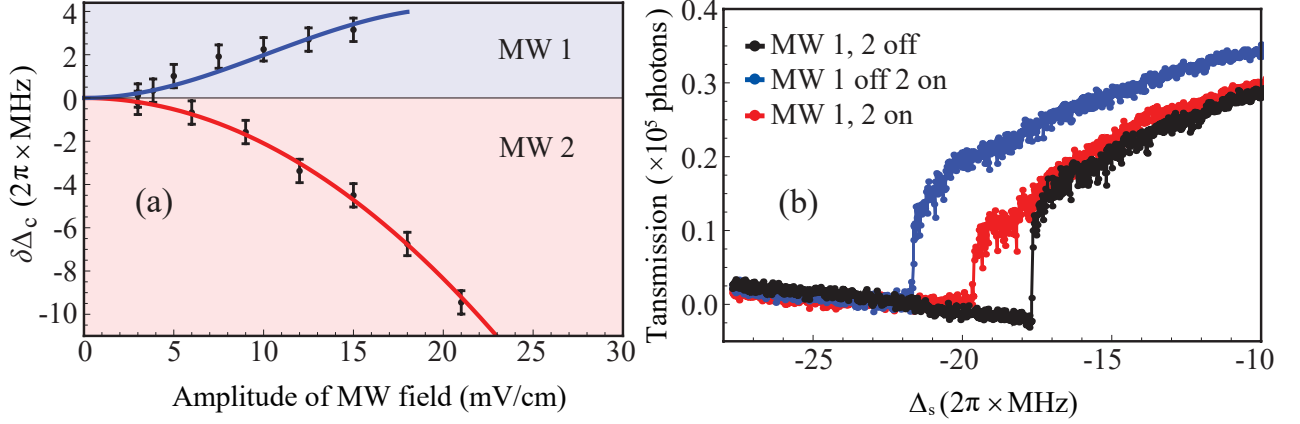


Figure S3. **Measurement of the shifted critical point.** (a) The measured frequency shifts at a transition point when coupled by the MW electric fields 1 and 2, respectively. The data are fit by Δ_D with a MW electric field broadening $-(\Delta_{mw}/2 \pm \sqrt{\Delta_{mw}^2 + \Omega_{mw}^2}/2) - \eta\Omega_{mw}^2$ ($\Omega_{mw} = \mu_{RF}E_{mw}/\hbar$) with experimental parameters (red) of $\Delta_{mw} = -2\pi \times 420$ MHz and a fitted broadening coefficient $\eta = 5.6 \times 10^{-4}$ MHz $^{-1}$ and parameters (blue) of $\Delta_{mw} = 2\pi \times 70$ MHz, $\eta = 2.2 \times 10^{-3}$ MHz $^{-1}$. Here $\mu_{RF} = 3320 ea_0$ is the dipole momentum of RF-transition $51D_{3/2} \rightarrow 50F_{5/2}$ or $51D_{3/2} \rightarrow 52P_{1/2}$, e is the electronic charge, and a_0 is the Bohr radius. (b) The measured phase transitions with the MW electric fields 1 off and 2 on (blue), and with the MW electric fields 1 and 2 both off (black), with the MW electric fields 1 and 2 both on (red). The frequencies of chosen RF transitions 1 and 2 are $f_{mw1} = 2\pi \times 16.60$ GHz for $52P_{1/2}$ and $f_{mw2} = 2\pi \times 17.22$ GHz for $50F_{5/2}$ respectively, and the intensities of the MW electric fields are set as $E_{mw1} = 7.8$ mV/cm and $E_{mw2} = 9.0$ mV/cm.

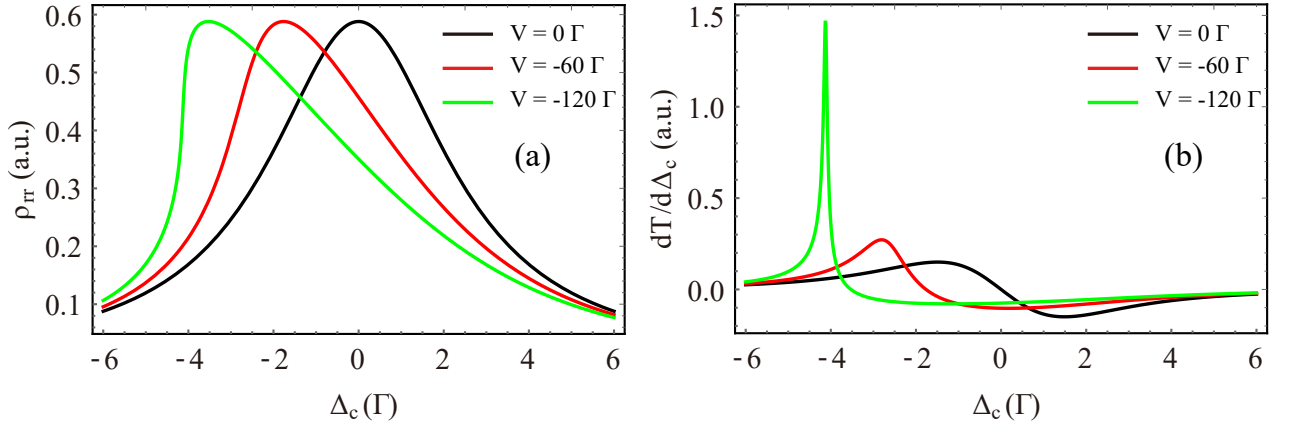


Figure S4. **Theoretical simulations of interacting three-level atoms.** (a) Rydberg state population ρ_{rr} as a function of laser detuning Δ for different interaction strengths V . (b) The derivative of Rydberg population with respect to Δ .

are decreased below the driving of the MW electric fields as explained above.

Three level model with mean field approximation. In our case, the model considered in the simulation is two level model which is slightly different from that in experiment. However, the phenomena uncovered by these two are the same. In Fig. S4, the population of Rydberg atoms with different interaction strength V varying with detuning of coupling light Δ_c and the corresponding derivative are also illustrated.

The three level model with mean field approximation is given in the following. The interaction of the EIT light fields with an ensemble of three level atoms is governed by

the master equation for the single atom density matrix,

$$\frac{d}{dt}\rho = -\frac{i}{\hbar}[H, \rho] + \frac{1}{\hbar}L[\rho] \quad (1)$$

where

$$H = -\frac{\hbar}{2} \begin{pmatrix} 0 & \Omega_p & 0 \\ \Omega_p & -2\Delta_p & \Omega_c \\ 0 & \Omega_c & -2(\Delta_p + \Delta_c) \end{pmatrix} \quad (2)$$

where $\Omega_{p(c)}$ and $\Delta_{p(c)}$ are the Rabi frequency and detuning of probe (coupling) light, respectively, and the Hilbert space is spanned by atomic ground state $|g\rangle$, excited intermediate state $|e\rangle$, and Rydberg state $|r\rangle$.

The Lindblad superoperator

$$L[\rho] = \frac{\hbar}{2} \begin{pmatrix} 2\Gamma_e \rho_{ee} & -\Gamma_e \rho_{ge} & -\Gamma_r \rho_{gr} \\ -\Gamma_e \rho_{eg} & -2\Gamma_e \rho_{ee} + 2\Gamma_r \rho_{rr} & -(\Gamma_r + \Gamma_e) \rho_{er} \\ -\Gamma_r \rho_{rg} & -(\Gamma_r + \Gamma_e) \rho_{re} & -2\Gamma_r \rho_{rr} \end{pmatrix} \quad (3)$$

where Γ_e and Γ_r accounts for the finite lifetime of $|e\rangle$ and $|r\rangle$.

In our mean field theory, the master equation is first solved in steady state, i.e., $d\rho/dt = 0$. Then the detuning of the coupling light is modified with mean field approximation ($\Delta_c \rightarrow \Delta_c - V\rho_{rr}$) and the equations are iterated until convergence of ρ_{rr} .

-
- [1] D.-S. Ding, H. Busche, B.-S. Shi, G.-C. Guo, and C. S. Adams, [Phys. Rev. X 10, 021023 \(2020\)](#).